Liquid jet and droplet deformation induced by non-uniform acoustics radiation pressure distribution

Rafael Herrera, Jean-Bernard Blaisot, Christine Richard, Françoise Baillot

Liquid jet and droplet deformation induced by non-uniform acoustics radiation pressure distribution

Rafael Herrera[1], Jean-Bernard Blaisot*[1], Christine Richard[2], Françoise Baillot[1]
[1]CORIA – UMR 6614, Normandie Université, Université et INSA de Rouen, Saint-Etienne du Rouvray, France
[2]LMRS – UMR 6085, Normandie Université, Université de Rouen, Saint-Etienne du Rouvray, France
*Corresponding author: blaisot@coria.fr

Abstract
The present work focuses on non linear acoustic effects on an elliptic cylinder or an ellipsoid. These effects are encountered in acoustic levitation, ultrasonic standing wave atomization or two-phase flow combustion instabilities. Theoretical approaches mainly paid attention on the total radiation force, but a modeling of the distribution of acoustic radiation pressure around the object is needed to predict liquid object deformation. In the present study, a semi-analytical model is presented in order to compute the local radiation pressure as the only reason for liquid jet or droplet deformation. The method used here imposes an incident field to, a posteriori, compute the scattered field as a function of the object geometrical properties. A partial wave decomposition(PWD) model is developed to express incident and scattered fields by and immovable object with rigid boundary conditions. Radiation pressure is computed for progressive and standing wave fields. Validation of our method is done by comparing with the radiation force results from the literature. Results show that the larger the deformation, the higher the acoustic effects in a direction perpendicular to the acoustic wave axis.

Keywords
Acoustics, radiation pressure, elliptic cylinder, ellipsoid.

Introduction

Non linear effects of acoustics are encountered in applications such as acoustic levitation, ultrasonic standing wave atomization or two-phase flow combustion instabilities occurring in rocket engines [1–4]. Most of the studies dealing with interaction of acoustics and spherical [5–9] or cylindrical [10–14] objects focused on the stationary radiation force. The main objective was there to determine the displacement of these objects. However, their deformation is also of a great interest in applications dealing with liquid objects. In studies on acoustically levitating droplets, some authors considered the radiation pressure distribution as the source of the stationnary deformation of the free surfaces [2, 15, 16]. They showed that spherical droplets became oblate when exposed to the radiation pressure. For cylindrical objects, it was experimentally proven that cylindrical liquid jets subjected to a low frequency standing wave were susceptible to be deformed into elliptic cylinders [17]. Thus, by relying on those results it appeared that knowing radiation pressure distribution around elliptic objects was necessary to correctly analyze the interaction between acoustics and deformed objects. Hasheminejad et al. [18, 19] developed an approach based on elliptic functions, namely Mathieu functions, to describe the acoustic scattered field. This is a powerful method, but limited in its applications due to the occurrence of Mathieu polynomials instability. Other authors considered a theoretical approach based on the expression of the incident and scattered waves by means of the formal cylindrical or spherical functions [17, 20–22].
All the studies cited above focused only on the modeling of the radiation force computed with the far field assumption avoiding the computation of radiation pressure distribution. To tackle the problem of object deformation induced by acoustics, it is needed to model the radiation pressure distribution. This is done here for elliptic cylinders and ellipsoids. The two-way coupling between incident acoustic harmonic plane waves and these objects is explored by computing the radiation pressure field and resulting radiation force. In the first section is presented the method used to compute the acoustic velocity potential field scattered by elliptic objects and the consequent computation of the radiation pressure and radiation force. Results showing the convergence of the method, its validation and the radiation pressure distribution are presented in the second section. Finally, the last section is dedicated to some conclusions.

Method

The method is applied to (progressive or standing) harmonic plane waves propagating in the direction $\vec{x}$ (see Figs. 1 and 2). Objects (cylinder or ellipsoid) present an elliptical cross section in the plane $(O, \vec{x}, \vec{y})$, with O the cross section center. $\vec{z}$ is either the cylinder main axis direction or that of the ellipsoid third semi-axis. The distance along $\vec{x}$ between O and a fixed plane of reference for the acoustic field is noted h. The incident field is expressed by its velocity potential field: $\hat{\phi}_i = \phi_0 e^{-i\omega t}\phi$ with $\phi = e^{ik(x+h)} + Re^{-ik(x+h)}$ and ϕ_0 is the amplitude of the potential acoustical field, ω the angular frequency and k the wave number. The wave reflecting coefficient R is 0 for a progressive wave and 1 for a standing wave. The position of a point is specified by its polar coordinates (r, θ) as

depicted in Figs. 1 and 2. The total field is computed as the superposition of the incident field ϕ_i and scattered field ϕ_s, i.e. $\phi_T = \phi_i + \phi_s$. For an object at rest the boundary condition is given by:

$$\left(\vec{\nabla}\phi_T \cdot \vec{n}\right)_{surface} = 0 \tag{1}$$

where $\vec{n} = \vec{e}_r - \frac{1}{r}\frac{dr}{d\theta}\vec{e}_\theta$ is the normal unit vector on the object surface. According to King [5] the radiation pressure for an object at rest is given by $P_{rad} = P_\phi + P_q$ where $P_\phi = -\frac{1}{2}\rho_0 \left\langle |\vec{\nabla}\phi_T|^2 \right\rangle$ and $P_q = \frac{1}{2}\frac{\rho_0}{c_0^2}\left\langle \left(\frac{\partial \phi_T}{\partial t}\right)^2 \right\rangle$ with ρ_0 and c_0 the surrounding fluid density and the sound velocity respectively and $\langle\cdot\rangle$ indicating time-averaging. Thus, P_ϕ and P_q are the time-averaged volumetric kinetic and potential acoustic energy densities respectively. The radiation force is deduced by integrating the radiation pressure field all over the object surface:

$$\overrightarrow{F}_{rad} = -\oint_S P_{rad}\,\overrightarrow{n}\,dS \tag{2}$$

where $dS = r(\theta)d\theta$ for elliptic cylindrical objects per unit length and $dS = 2\pi r^2(\theta)\sin\theta d\theta$ for ellipsoids symmetric with respect to the acoustic axis. The method employed to compute scattered field uses cylindrical or spherical functions to describe the incident and scattered fields, as proposed in Mitri's papers [21, 22]. The scattered field is semi-analytically calculated as a dependence of the incident field and the object geometry. The incident plane wave $\phi_i(r,\theta)$ and the scattered $\phi_s(r,\theta)$ field are expressed as infinite series of functions whose form depends on the object geometry. The definition of ϕ_s includes a vector of unknowns $[C_n]$ which is obtained by solving a linear system of equations resulting from the boundary condition expressed by Eq. 1. A PYTHON 3 code has been developed to solve the linear system using a full rank matrix solver of the SCYPY linear algebra library. Once the scattered coefficient is known, the scattered field, and consequently the total field ϕ_T, is obtained. The radiation pressure distribution, P_{rad} is calculated with P_ϕ and P_q and the resulting radiation force is given by computing Eq. 2. Results for standing waves are given for $h = \frac{\lambda}{8}$, corresponding to an intensity anti-node (IAN) where the product of the acoustic velocity with the acoustic pressure (surface energy flux) is maximum. This choice is motivated by the experimental results of Ficuciello [23] and by the numerical results of Mitri [21, 22] that serve as reference for our computation. For progressive waves, results are not dependent on the location of the object in the acoustic field.

Elliptic cylindrical objects

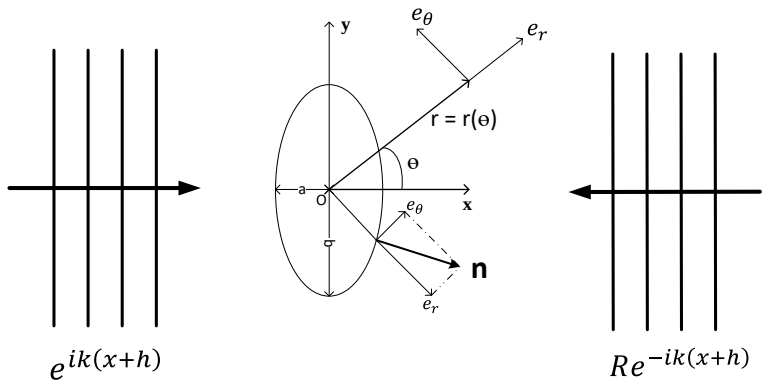

Figure 1. Geometric configuration for an elliptic cylinder interacting with acoustical plane waves.

For an elliptic cylinder ϕ_i is given by Eq. 3:

$$\phi_i = \sum_{n=0}^{\infty} e_n A_n^{qst} i^n J_n(kr)\cos n\theta \tag{3}$$

J_n is the Bessel function of first kind of order n and $A_n^{qst} = e^{ikh} + R(-1)^n e^{-ikh}$. The coefficient e_n is equal to 1 for $n = 0$ and 2 for $n \neq 0$. A usual series expansion for the scattered field in cylindrical coordinates is:

$$\phi_s = \sum_{n=0}^{\infty} e_n i^n C_n H_n^1(kr)\cos n\theta \tag{4}$$

H_n^1 is the Hankel function of the first kind of order n. $[C_n]$ is the unknown scattered coefficient vector.

The boundary condition expressed by substituting ϕ_T with Eqs. 3 and 4 in Eq.1 leads to:

$$\sum_{n=0}^{\infty} [\Gamma_n(\theta) + C_n \gamma_n(\theta)] = 0 \tag{5}$$

with

$$\Gamma_n(\theta) = e_n i^n A_n^{qst} \left[k J_n'(kr) \cos\theta + \frac{n}{r^2} J_n(kr) \sin n\theta \right] \tag{6}$$

$$\gamma_n(\theta) = e_n i^n \left[k H_n'(kr) \cos\theta + \frac{n}{r^2} H_n(kr) \sin n\theta \right] \tag{7}$$

In order to obtain C_n, Eq.5 is expanded by means of cosines series as follows:

$$\sum_{n=0}^{\infty} [\Gamma_n(\theta) + C_n \gamma_n(\theta)] = \sum_{l=0}^{\infty} i^l e_l (\psi_l \cos l\theta + \beta_l \cos l\theta) = 0 \tag{8}$$

Coefficients ψ_l and β_l are obtained by using the cosines product orthogonality property:

$$\psi_l = \int_0^{2\pi} \frac{\sum_{n=0}^{\infty} [\Gamma_n(\theta)] \cos l\theta}{e_l i^l |\cos l\theta|} d\theta \tag{9}$$

$$\beta_l = \int_0^{2\pi} \frac{\sum_{n=0}^{\infty} [C_n \gamma_n(\theta)] \cos l\theta}{e_l i^l |\cos l\theta|} d\theta \tag{10}$$

Coefficients β_l are expressed by a matrix product $\beta_l = [\eta_n^l] \cdot [C_n]$ where $[C_n]$ is the unknown coefficient column vector and each component of the matrix $[\eta_n^l]$ is given by Eq. 11:

$$\eta_n^l = \int_0^{2\pi} \frac{\gamma_n(\theta) \cos l\theta}{e_l i^l |\cos l\theta|} d\theta \tag{11}$$

Ellipsoidal objects

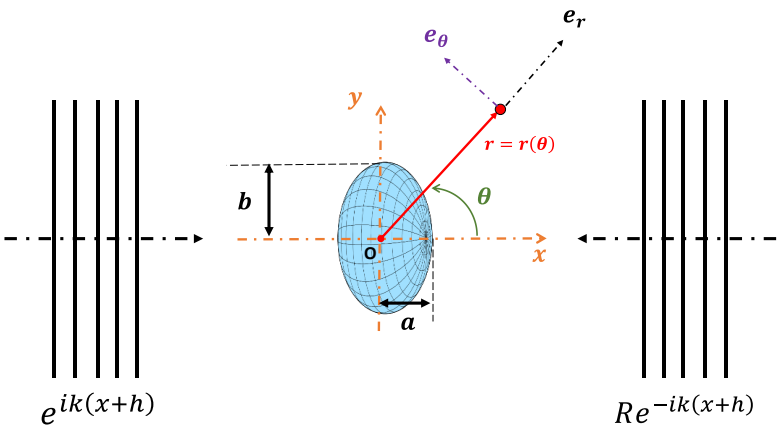

Figure 2. Geometric configuration for an ellipsoid interacting with acoustical plane waves.

In this part we consider an ellipsoid symmetric with respect to the acoustic axis, with only two independent semi-axes. Thus, as for the elliptic cylinder, the physical quantities are thus described by r and θ (see Fig. 2). For the ellipsoid ϕ_i is given by Eq. 12:

$$\phi_i(r,\theta) = \sum_{n=0}^{\infty} (2n+1) A_n^{qst} i^n j_n(kr) P_n(\cos\theta) \tag{12}$$

where $j_n(kr)$ is the first kind spherical Bessel function of order n, and $P_n(\cos\theta)$ is the Legendre polynomial of order n. The scattered field is written by using the spherical functions as well:

$$\phi_s(r,\theta) = \sum_{n=0}^{\infty} (2n+1) i^n C_n h_n(kr) P_n(\cos\theta) \tag{13}$$

where $h_n(kr)$ is the first kind spherical Hankel function of order n. By substituting for Eqs.12 and 13 in the boundary

condition (Eq.1), the following relationship is obtained:

$$\sum_{n=0}^{\infty} \left[\Gamma_n(\theta) + C_n\gamma_n(\theta)\right] = \sum_{l=0}^{\infty} (2l+1)\, i^l (\psi_l P_l(\cos\theta) + \beta_l P_l(\cos\theta)) = 0 \tag{14}$$

where functions Γ_n and γ_n are defined as follows:

$$\Gamma_n(\theta) = (2n+1)\, i^n A_n^{qst} \left[kj_n'(kr) P_n(\cos\theta) + \frac{\sin\theta}{r^2}\, j_n(kr)\, \frac{dP_n(\cos\theta)}{d(\cos\theta)} \right] \tag{15}$$

$$\gamma_n(\theta) = (2n+1)\, i^n \left[kh_n'(kr) P_n(\cos\theta) + \frac{\sin\theta}{r^2}\, h_n(kr)\, \frac{dP_n(\cos\theta)}{d(\cos\theta)} \right] \tag{16}$$

The coefficients ϕ_l and β_l are obtained by means of the Legendre polynomials orthogonality property [*]:

$$\psi_l = \int_0^{\pi} \sum_{n=0}^{\infty} \left[\Gamma_n(\theta)\right] i^{-l} P_l(\cos\theta) d\theta \tag{17}$$

$$\beta_l = \int_0^{\pi} \sum_{n=0}^{\infty} \left[C_n\gamma_n(\theta)\right] i^{-l} P_l(\cos\theta) d\theta \tag{18}$$

By considering β_l as the scalars resulting from the matrix product between $[C_n]$ and $\left[\eta_n^l\right]$, the following expression is established:

$$\eta_n^l = \int_0^{\pi} \gamma_n(\theta) i^{-l} P_l(\cos\theta) d\theta \tag{19}$$

A similar linear system as for elliptic cylinders is obtained. Radiation pressure and force are then computed as indicated in the method section.

Results and discussion

Radiation pressure on elliptic cylinders

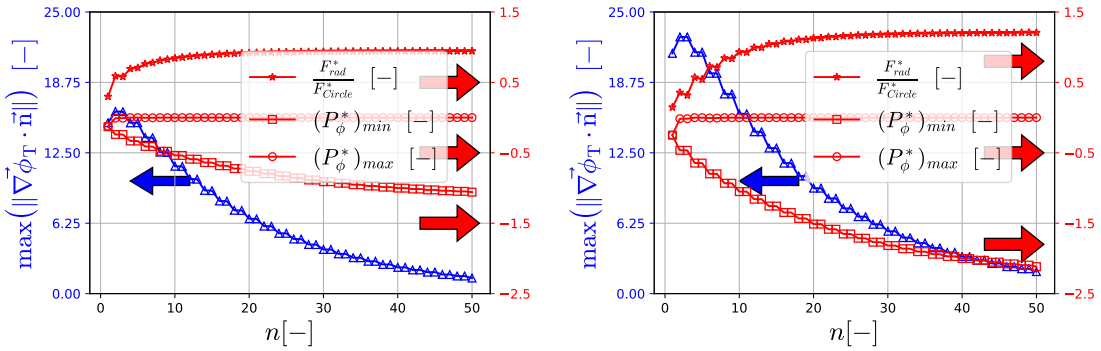

(a) Standing wave, IAN ($h = \frac{\lambda}{8}$)

(b) Progressive wave

Figure 3. Convergence of the scattered field computation for an elliptic cylinder with $\epsilon = 0.5$ as a function of the number of terms.

Radiation pressure and force are expressed in their dimensionless forms $P^*_{rad} = \frac{P_{rad}}{\overline{P}}$ and $F^*_{rad} = \frac{F_{rad}}{\overline{P}b}$ where $\overline{P} = \rho_0 \phi_0^2 k^2$ is the averaged-time acoustic energy per unit volume of the free progressive wave. The elliptic geometry is specified by the aspect ratio, $\epsilon = a/b$ and the cross section area $\pi ab = \pi D_0^2/4$ is set to the one of the associated circular cylinder which serves as a reference. The expression of the radiation force for a small cylindrical cylinder ($\alpha = \frac{D_0}{2}k << 1$) proposed by Ficuciello [23] is then taken as a reference too: $F^*_{Circle} = \frac{3}{4}\pi\alpha \sin 2kh$ for standing waves and $F^*_{Circle} = \frac{5}{8}\pi^2\alpha^3$ for progressive waves. Calculations are done for a standing wave at location $h = \frac{\lambda}{8}$ (IAN) and for a progressive wave. Infinite series (Eq. 5) were reduced to a finite number of terms ($n_{max} = 50$) due to the accuracy limitation of the code for huge numbers (10^{308}). Convergence of the scattered field computation for $\epsilon = 0.5$ is shown in Fig. 3(a) for a standing wave and in Fig. 3(b) for a progressive wave. Blue symbols (Δ) indicate the maximum value, $max(|\vec{\nabla}\phi_T \cdot \vec{n}|)$ taken from the boundary condition (Eq.1) on the object surface. Red symbols (o) and (□) show the evolution of the maximum and minimum values of the radiation pressure term P^*_ϕ. Finally, symbols($*$) represent the ratio of the radiation force for an elliptic cylinder to the one for a circular cylinder $\frac{F^*_{rad}}{F^*_{Circle}}$.

[*] $\int_0^{\pi} P_l(\cos\theta) P_n(\cos\theta) d\theta = \frac{1}{(2n+1)}\delta_{ln}$

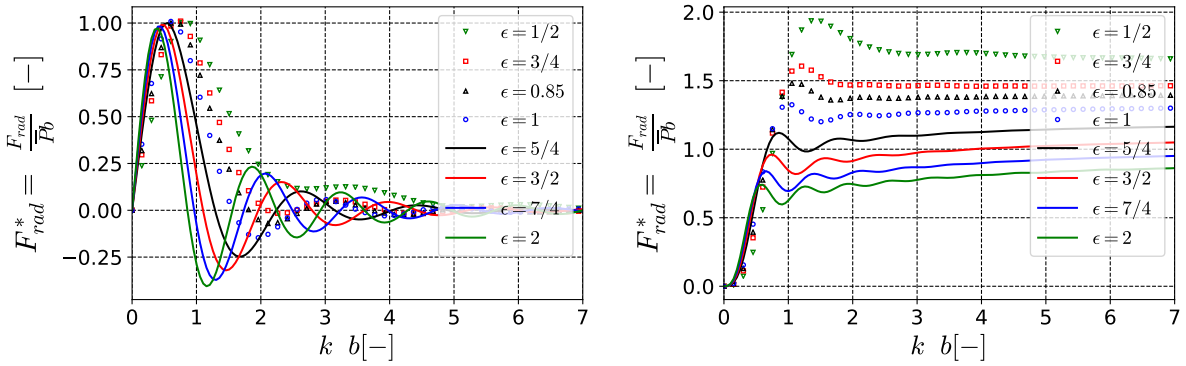

(a) Standing wave, IAN ($h = \frac{\lambda}{8}$)

(b) Progressive wave

Figure 4. Dimensionless radiation force for an elliptic cylinder as a function of the dimensionless number $\alpha = kb$ for some values of ϵ.

For both waves, the target value for Eq. 1 $max(|\vec{\nabla}\phi_T \cdot \vec{n}|) = 0)$ is not reached but it can be observed that the convergence of the radiation quantities is well attained. Note that the evolution of P_q^* is not shown since the convergence is found whatever n.

Figs.4(a) and 4(b) present the values of the dimensionless radiation force F^*_{rad}, once calculations converge. All the tests conditions (ϵ and range for the ordinate kb) are the same as those proposed by Mitri in [21]. For both types of waves, our results perfectly match with Mitri's results which were computed under the far field consideration. This comparison validates our approach.

This first step gives the necessary confidence to pursue the present development in order to compute the radiation pressure distribution, especially on the object surface. The results for the dimensionless quantity P^*_{rad} are illustrated for an elliptical cylinder in Fig.5(a) at an intensity anti-node of a standing wave and in Fig.5(b) for a progressive wave. Results perfectly match the radiation pressure distribution found by Ficuciello [23] for a circular cylinder corresponding to $\epsilon = 1$. For standing waves (figure 5(a)), the maximum compression effect ($P^*_{rad} = 0.15$) is obtained for $\theta = 180°$ and another local maximum ($P^*_{rad} = 0.10$) is found $\theta = 0°$ regardless of ϵ, both locations being on the acoustic axis. The difference between these two compression effects is of the order of α. For the positions nearby $\theta = 90°$ and $\theta = 270°$ suction effects are maximum and they increase as ϵ decreases. Thus for an elliptic cross section elongated perpendicularly to the acoustic axis, the suction effects are more efficient. A similar behavior is noted for progressive waves (figure 5(b)). The main differences compared to results at (IAN) are: i) the difference between compression maximums for $\theta = 0°$ and $180°$ is smaller ($\simeq \alpha^3$); ii) the maximum suction effect is more pronounced and is exactly located at $\theta = 90°$ and $270°$. Compression and suction effects are thus more efficient in the case of a progressive wave than for a standing wave at IAN. However, for other object locations in the standing wave different conclusions can be obtained. A schematic representation of the radiation pressure

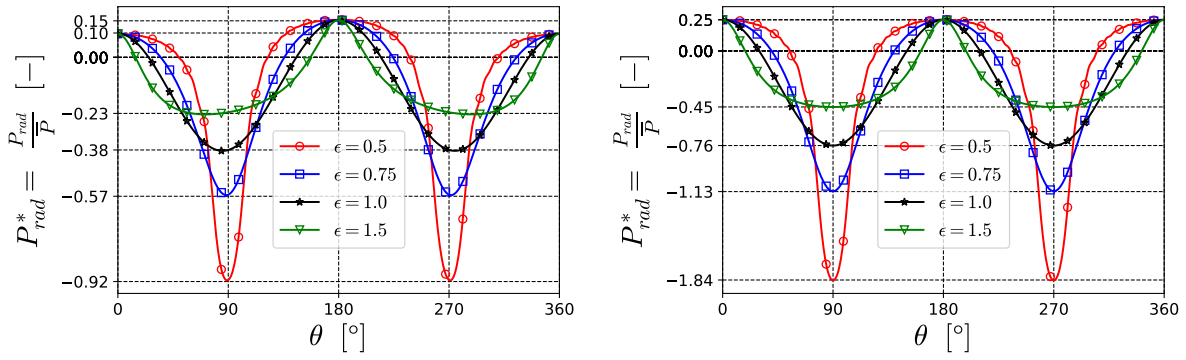

(a) Standing wave, IAN ($h = \frac{\lambda}{8}$)

(b) Progressive wave

Figure 5. Dimensionless radiation pressure for an elliptic cylinder as a function of the polar coordinate θ.

distribution at an intensity anti-node ($h = \frac{\lambda}{8}$) of a standing wave is shown in Fig.6 which highlights how an elliptic cylinder with its minor semi-axis in the perpendicular plane (P.P) becomes an elliptic cylinder with its major semi-axis in the plane (P.P) via a circular cylinder. It can be observed that as $\epsilon \to 0$ compression effects extend more and more around the object surface where the curvature becomes smaller and smaller without compression maximum values being fundamentally changed, whereas suction effects, gathered around the apices $\theta = 90°$ and $\theta = 270°$, strongly increase while the curvature also strongly increases.

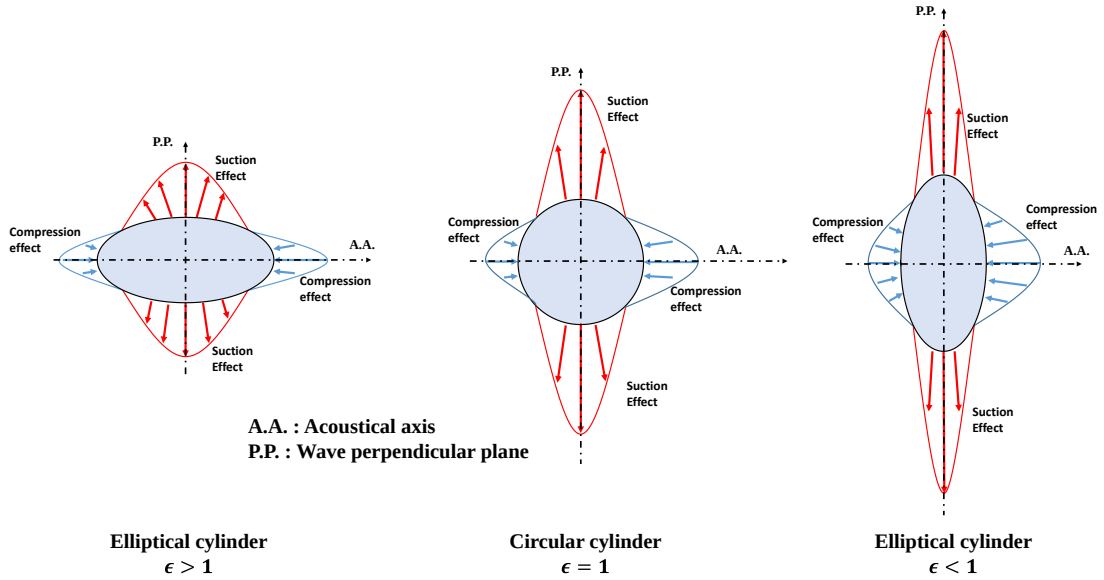

Figure 6. Schematic representation of the radiation pressure distribution on the surface of an elliptic cylinder for three kinds of ellipticity ($\epsilon > 1$, $\epsilon = 1$ and $\epsilon < 1$).

Radiation pressure on ellipsoids

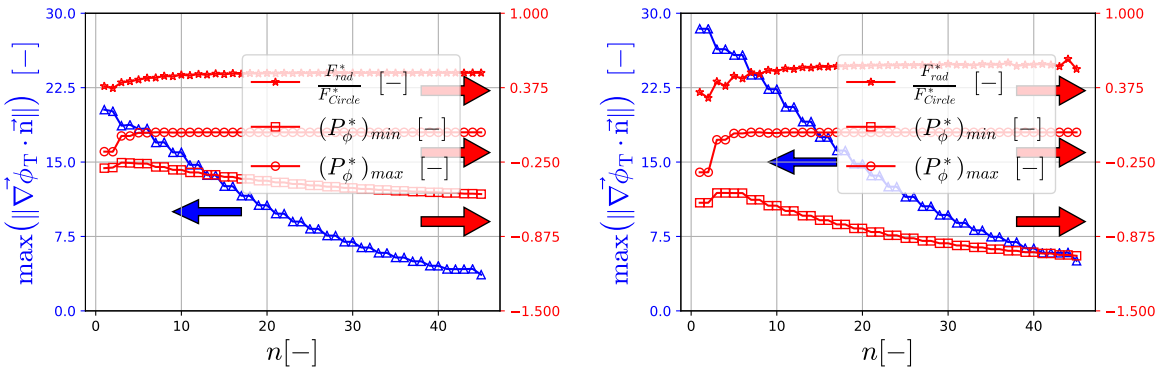

(a) Standing wave, IAN ($h = \frac{\lambda}{8}$)

(b) Progressive wave

Figure 7. Convergence of the scattered field computation for an ellipsoid with $\epsilon = 0.5$ as a function of the number of terms.

In the case of an ellipsoid object, the non-dimensional expression for the radiation pressure remains the same as in previous section and the non-dimensional radiation force is given by $F^*_{rad} = \frac{F_{rad}}{\overline{P}b^2}$. The volume of the ellipsoid is set to a constant equal to the volume of the spherical object of diameter D_0, serving as a reference. Therefore, the 3 semi-axes of the ellipsoid can be obtained as a function of the aspect ratio $\epsilon = \frac{a}{b}$, i.e. $a = \frac{D_0}{2}\epsilon^{2/3}$ and $b = c = \frac{D_0}{2\epsilon^{1/3}}$. Analytic expressions for the radiation force were proposed by Ficuciello [23] for small spherical objects ($\alpha = \frac{D_0}{2}k << 1$) placed in a standing wave $F_{Sphere} = \frac{5}{6}\pi\alpha \sin 2kh$ or in a plane harmonic progressive waves : $F_{Sphere} = \frac{11}{18}\pi\alpha^4$. Calculations are done for a standing wave at location $h = \frac{\lambda}{8}$ (IAN) and for a progressive wave. Convergence of the scattered field for an ellipsoid with $\epsilon = 0.5$ is shown in Fig. 7(a) for a standing wave and in Fig. 7(b) for a progressive wave. For both waves, the target value ($max(|\vec{\nabla}\phi_T \cdot \vec{n}|) = 0$) is not reached as for elliptic cylinder, but the convergence of the radiation quantities is well attained. As for the elliptic cylinder, the convergence is found whatever n for P^*_q. Figs.8(a) and 8(b) present the values of the dimensionless radiation force, F^*_{rad} once calculations converge. All the tests conditions (ϵ and range for the ordinate kb) are the same as those proposed by Mitri in [22]. For both types of waves, our results perfectly match with Mitri's results which were computed under the far field consideration. This comparison validates here again our approach. As previously, this first step gives the necessary confidence to compute the radiation pressure distribution. Results for P^*_{rad} are illustrated in Fig.9(a) for an ellipsoid at an intensity anti-node (IAN) of a standing wave and in Fig.9(b) for a progressive wave. Here again

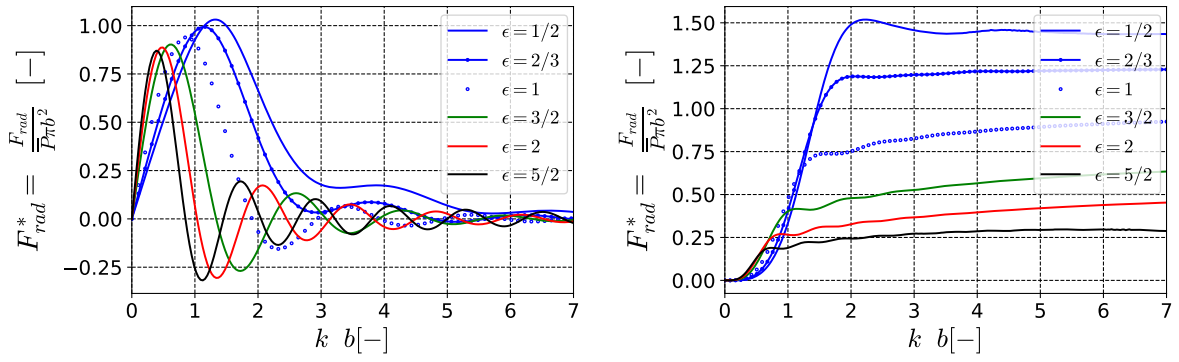

(a) Standing wave, IAN ($h = \frac{\lambda}{8}$)

(b) Progressive wave

Figure 8. Dimensionless radiation force for an ellipsoid as a function of the dimensionless number $\alpha = kb$ for some values of ϵ.

results perfectly match with the radiation pressure distribution found by Ficuciello [23] for a sphere corresponding to $\epsilon = 1$. The radiation pressure distribution is similar to that obtained in the case of an elliptic cylinder in a standing wave or in a progressive waves. Compression effects are maximum at points placed on the acoustic axis ($\theta = 0°$ and $180°$) and suction effects are maximum nearby or at the positions $\theta = 90°$ and $270°$ for standing and progressive waves respectively. Moreover, it is also verified that suction effect maximum increases when ϵ decreases while compression maximum is independent of ϵ. If the compression maximums are exactly the same for both elliptic configurations, the maximum absolute value for the suction effect is 42.4% lower for ellipsoids than for cylinders. The previous results can be also summarized by means of Fig. 6 which is still valid.

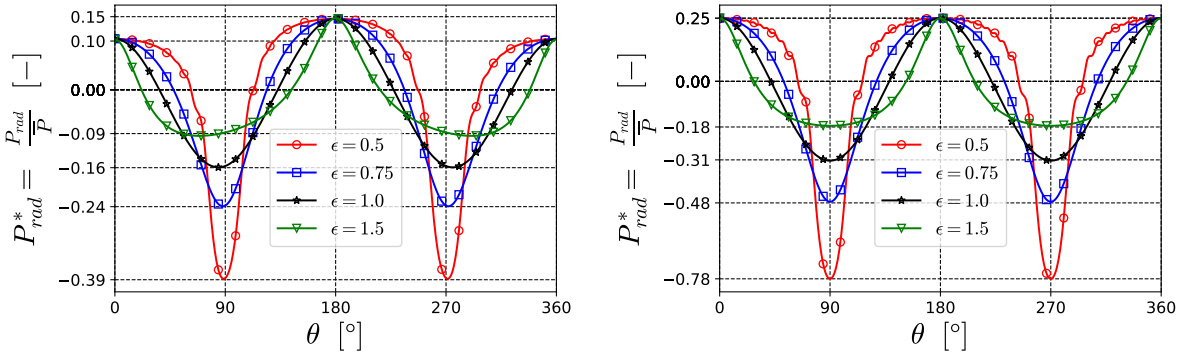

(a) Standing wave, IAN ($h = \frac{\lambda}{8}$)

(b) Progressive wave

Figure 9. Dimensionless radiation pressure for an ellipsoid as a function of the polar coordinate θ.

Conclusions

The present study was motivated by experimental observations of liquid jets, ligament or spherical droplets transformed into elliptic cylinders or into ellipsoids by acoustics (see [2–4, 15–17]). The first milestone presented in that paper aims for simulating the interaction of a plane harmonic (standing or progressive) wave with an elliptical cylinder or an ellipsoid, by establishing the radiation pressure distribution all over the object surface (and beyond), and by determining the resulting radiation force. The acoustic field is computed by means of a semi-analytic method based on infinite cylindrical or spherical functions series which model the incident as well as the scattered acoustic velocity potentials. Results concerning standing waves are illustrated at an intensity anti-node (IAN) location. The present "near field" method was validated for both types of object geometry by successfully comparing the radiation force (obtained by integrating the radiation pressure over the object surface) with Mitri's results obtained by a "far field" approach [21, 22].

Similar properties have been found for elliptic cylinders and ellipsoids placed either at IAN of a standing wave or in a progressive wave. In particular, regardless of the aspect ratio ϵ, object surface points situated on the acoustic axis (A.A.) are always submitted to a constant maximum compression. In the near vicinity of the wavefront (P.P.) containing the object center, suction effects are always maximum and they increase as ϵ decreases. Suction effects have been shown to be more efficient when the major semi-axis is contained in (P.P.) than aligned with (A.A.).

Finally, as $\epsilon \to 0$ compression effects spread over a larger area of the object surface. This comes with a diminishing of the curvature without compression maximum values being essentially changed. On the other hand, suction effects always remain located near (P.P.) and strongly increase as the curvature strongly increases too. This important

feature suggests that when a liquid cylinder or droplet is being deformed by acoustics, the radiation effects are simultaneously enhanced over its surface, resulting in a bigger deformation. This corresponds to the progressive flattening of a liquid jet perpendicular to (A.A) already mentioned by Ficuciello et al. [4]. Indeed, in application to liquid-gas interface deformation the acoustic effects are counterbalanced by surface tension forces. The present analysis does not take into account surface tension but this will be the subject of a future study.

Bibliography

[1] O. Andersen, S. Hansmann, and K. Bauckhage, "Production of fine particles from melts of metals or highly viscous fluids by ultrasonic standing wave atomization," *Particle & Particle Systems Characterization*, vol. 13, no. 3, pp. 217–223, 1996.

[2] A. L. Yarin, M. Pfaffenlehner, and C. Tropea, "On the acoustic levitation of droplets," *J. Fluid Mech.*, vol. 356, pp. 65–91, 1998.

[3] F. Baillot, J.-B. Blaisot, G. Boisdron, and C. Dumouchel, "Behaviour of an air-assisted jet submitted to a transverse high-frequency acoustic field," *Journal of Fluid Mechanics*, vol. 640, pp. 305–342, 2009.

[4] A. Ficuciello, J. Blaisot, C. Richard, and F. Baillot, "Investigation of air-assisted sprays submitted to high frequency transverse acoustic fields: Droplet clustering," *Physics of Fluids*, vol. 29, no. 6, p. 067103, 2017.

[5] L. V. King, "On the acoustic radiation pressure on spheres," in *Proceedings of the Royal Society of London A: Mathematical, Physical and Engineering Sciences*, vol. 147, pp. 212–240, The Royal Society, 1934.

[6] T. F. W. Embleton, "Mean force on a sphere in a spherical sound field. i. (theoretical)," *The Journal of the Acoustical Society of America*, vol. 26, no. 1, pp. 40–45, 1954.

[7] P. Glynne-Jones, P. P. Mishra, R. J. Boltryk, and M. Hill, "Efficient finite element modeling of radiation forces on elastic particles of arbitrary size and geometry," *The Journal of the Acoustical Society of America*, vol. 133, no. 4, pp. 1885–1893, 2013.

[8] F. G. Mitri, "Acoustic radiation force due to incident plane-progressive waves on coated spheres immersed in ideal fluids," *The European Physical Journal B - Condensed Matter and Complex Systems*, vol. 43, no. 3, pp. 379–386, 2005-02.

[9] S. Sepehrirahnama, K.-M. Lim, and F. S. Chau, "Numerical study of interparticle radiation force acting on rigid spheres in a standing wave," *The Journal of the Acoustical Society of America*, vol. 137, no. 5, pp. 2614–2622, 2015.

[10] F. Cai, L. Meng, C. Jiang, Y. Pan, and H. Zheng, "Computation of the acoustic radiation force using the finite-difference time-domain method," *The Journal of the Acoustical Society of America*, vol. 128, no. 4, pp. 1617–1622, 2010.

[11] D. Haydock, "Calculation of the radiation force on a cylinder in a standing wave acoustic field," *Journal of Physics A: Mathematical and General*, vol. 38, no. 15, pp. 3279–3285, 2005.

[12] F. G. Mitri, "Theoretical calculation of the acoustic radiation force acting on elastic and viscoelastic cylinders placed in a plane standing or quasistanding wave field," *The European Physical Journal B - Condensed Matter and Complex Systems*, vol. 44, no. 1, pp. 71–78, 2005.

[13] J. Wu, G. Du, S. S. Work, and D. M. Warshaw, "Acoustic radiation pressure on a rigid cylinder: an analytical theory and experiments," *The Journal of the Acoustical Society of America*, vol. 87, no. 2, pp. 581–586, 1990.

[14] A. Zhuk, "Radiation force acting on a cylindrical particle in a sound field," *International Applied Mechanics*, vol. 22, no. 7, pp. 689–693, 1986.

[15] A. L. Yarin, D. A. Weiss, G. Brenn, and D. Rensink, "Acoustically levitated drops: drop oscillation and break-up driven by ultrasound modulation," *International Journal of Multiphase Flow*, vol. 28, no. 6, pp. 887 – 910, 2002.

[16] C. P. Lee, A. V. Anilkumar, and T. G. Wang, "Static shape of an acoustically levitated drop with wave–drop interaction," *Physics of Fluids*, vol. 6, no. 11, pp. 3554–3566, 1994.

[17] P. L. Marston, W. Wei, and D. B. Thiessen, "Acoustic radiation force on elliptical cylinders and spheroidal objects in low frequency standing waves," in *AIP Conference Proceedings*, vol. 838, 2006.

[18] S. M. Hasheminejad and R. Sanaei, "Acoustic radiation force and torque on a solid elliptic cylinder," *Journal of Computational Acoustics*, vol. 15, no. 3, pp. 377–399, 2007.

[19] S. M. Hasheminejad and R. Sanaei, "Ultrasonic scattering by a fluid cylinder of elliptic cross section, including viscous effects," *IEEE Transactions on Ultrasonics, Ferroelectrics, and Frequency Control*, vol. 55, no. 2, pp. 391–404, 2008-02.

[20] F. Léon, F. Chati, and J. M. Conoir, "Acoustic scattering by an elastic elliptic cylinder in water: numerical results and experiments," *Ultrasonics*, vol. 42, no. 1, pp. 297 – 300, 2004.

[21] F. G. Mitri, "Acoustic radiation force on a rigid elliptical cylinder in plane (quasi)standing waves," *J. Appl. Phys.*, vol. 118, no. 214903, 2015.

[22] F. G. Mitri, "Acoustic radiation force on oblate and prolate spheroids in besselbeams," *Wave Motion*, vol. 57, pp. 231–238, 2015.

[23] A. Ficuciello, *Analyse des effets acoustiques à haute fréquence/haute intensité sur l'injection coaxiale: application aux moteurs-fusées*. phdthesis, Université de Rouen-Normandie, 2017.